RESEARCH

Bio-inspired biorthogonal compartmental microparticles for tumor chemotherapy and photothermal therapy

Qingfei Zhang[1,2], Gaizhen Kuang[1,2], Li Wang[2], Lu Fan[2], Yechao Zhou[1], Luoran Shang[4*], Yuanjin Zhao[1,3*] and Weijian Sun[1*]

Abstract

Microcarrier is a promising drug delivery system demonstrating significant value in treating cancers. One of the main goals is to devise microcarriers with ingenious structures and functions to achieve better therapeutic efficacy in tumors. Here, inspired by the nucleus-cytoplasm structure of cells and the material exchange reaction between them, we develop a type of biorthogonal compartmental microparticles (BCMs) from microfluidics that can separately load and sequentially release cyclooctene-modified doxorubicin prodrug (TCO-DOX) and tetrazine-modified indocyanine green (Tz-ICG) for tumor therapy. The Tz-ICG works not only as an activator for TCO-DOX but also as a photothermal agent, allowing for the combination of bioorthogonal chemotherapy and photothermal therapy (PTT). Besides, the modification of DOX with cyclooctene significantly decreases the systemic toxicity of DOX. As a result, the developed BCMs demonstrate efficient in vitro tumor cell eradication and exhibit notable tumor growth inhibition with favorable safety. These findings illustrate that the formulated BCMs establish a platform for bioorthogonal prodrug activation and localized delivery, holding significant potential for cancer therapy and related applications.

Keywords Microfluidics, Compartmental microparticle, Biorthogonal chemistry, Chemotherapy, Photothermal therapy
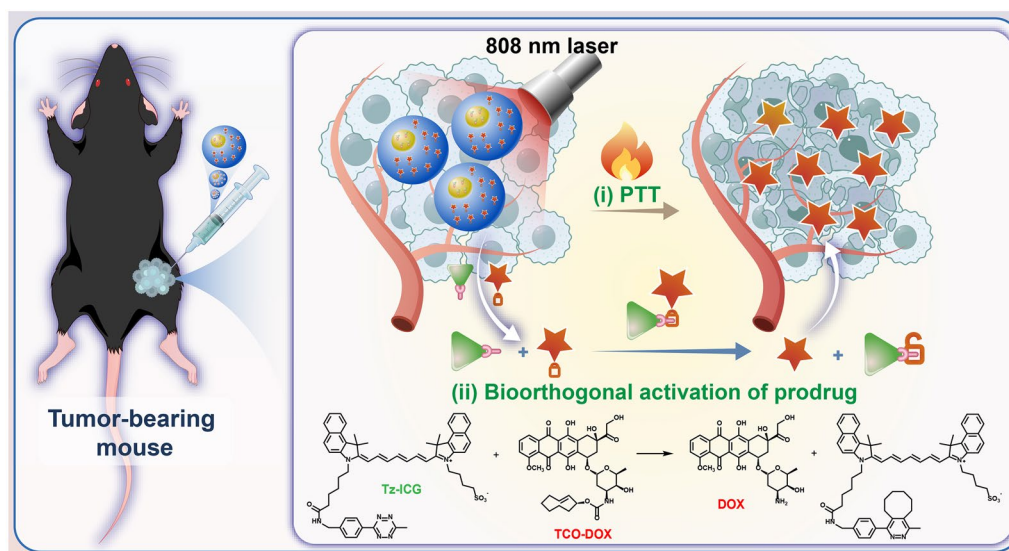
*Correspondence:
Luoran Shang
luoranshang@fudan.edu.cn
Yuanjin Zhao
yjzhao@seu.edu.cn
Weijian Sun
fame198288@126.com
Full list of author information is available at the end of the article

Zhang *et al. Journal of Nanobiotechnology*   (2024) 22:498

Page 2 of 12

Graphical Abstract

Introduction

Cancer is a significant global public health issue that profoundly impacts human lives and well-being [1–3]. Chemotherapy is among the main methods of tumor treatment, which kills cells directly through chemotherapeutic drugs [4, 5]. However, systemic administration of the drugs leads to low tumor accumulation, resulting in suboptimal drug utilization [6, 7]. Besides, chemotherapy is commonly linked to significant toxicity and adverse effects and frequently falls short of achieving an optimal therapeutic outcome via standalone treatment [8, 9]. In recent years, phototherapies, including photothermal (PTT) and photodynamic therapy, have garnered significant interest due to their minimal invasiveness, high spatiotemporal selectivity, and controllability [10–12]. By combining phototherapies with traditional chemotherapy, various drug delivery carriers such as films, hydrogels, fibers, etc. have been developed [13–16]. Although with promising therapeutic effects, these carriers still face many problems that limit their further application. Simple mixing of the drug and carrier material tends to result in insufficient control of the drug release behavior [17–19]. Besides, therapeutic drugs with intrinsic toxicity released from these carriers inevitably cause damage to normal tissue [20, 21]. Therefore, there is a promising prospect in developing an ingenious microcarrier with smart drug release and novel therapeutic options for the treatment of tumors.

In this paper, inspired by the nucleus-cytoplasm structure of cells and the material exchange reaction between them, we developed a type of biorthogonal compartmental microparticles loading biorthogonal reaction agents with sequential release abilities from microfluidics (Fig. 1). The nucleus and cytoplasm in the cell have different structures and functions and work together to maintain the cell's normal functioning. Inspired by this specific structure, biomimetic drug delivery systems have been developed for disease treatment [22–24]. Recently, bioorthogonal chemistry as a highly effective tool in chemical biology, has attracted much attention in various biomedical areas [25–29]. Inverse electron-demand Diels–Alder (IEDDA) reactions are typically bioorthogonal reactions that do not require metal catalysis [30]. By employing tetrazine structure components in Diels–Alder cycloadditions with high-tension cycloalkenes, these reactions demonstrate exceptional potential in various applications such as precise biomolecular labeling, synthesis of antibody–drug conjugates, prodrug activation, etc. [31–33] In addition, microfluidic technology enables the preparation of structural tunable microcarriers, which have broad applications in drug delivery and disease treatment [34–40]. It combines essential operational components, such as sample mixing, reaction, and separation onto a microfluidic chip. In particular, microfluidic electrospray is a precisely controllable technology with a wide range of application prospects [41, 42]. This technology utilizes electrical shear stress to produce droplets that are subsequently ejected into a solidifying solution to fabricate microparticles [43, 44]. Nowadays, microfluidic electrospray is commonly
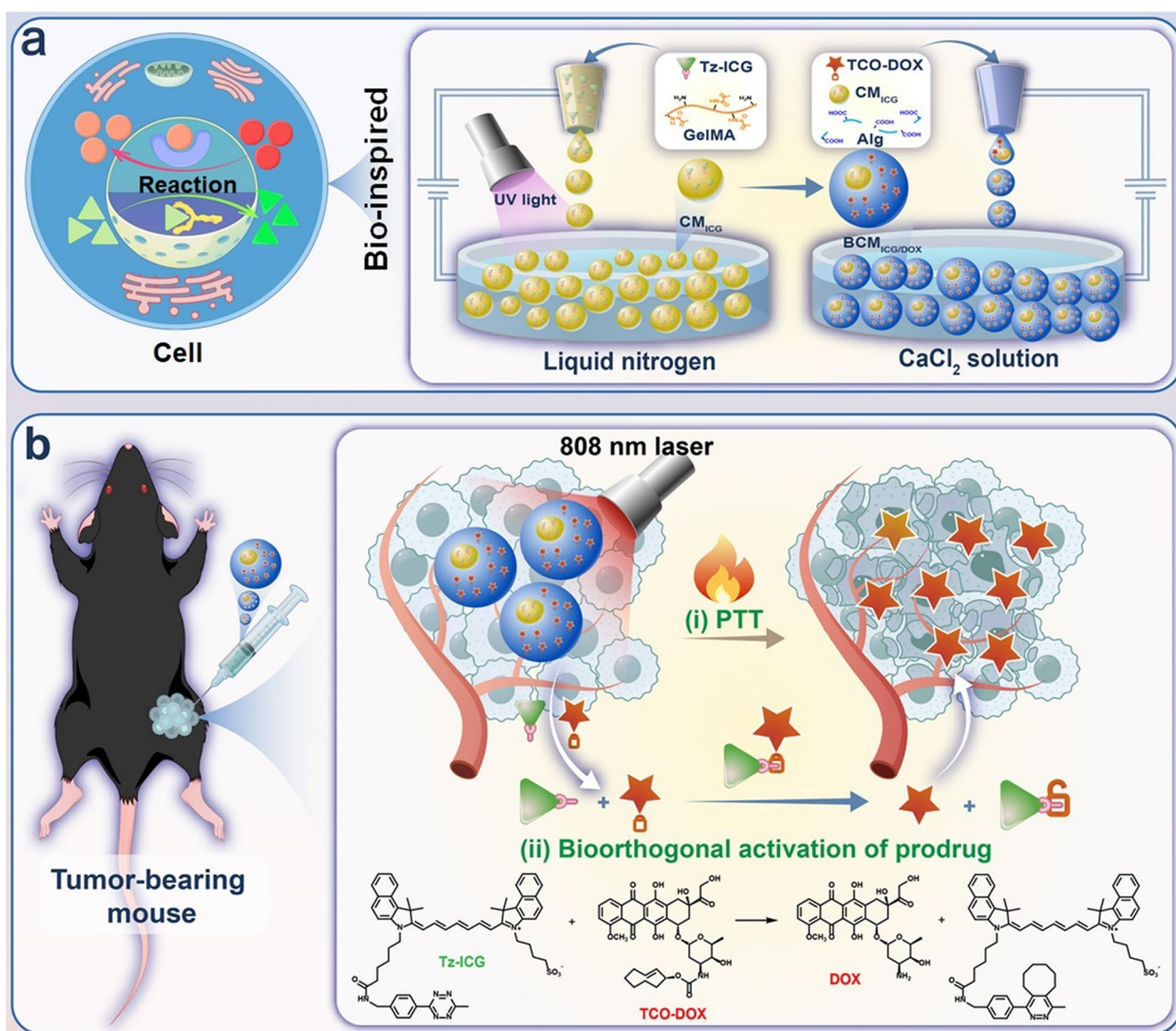
Zhang *et al. Journal of Nanobiotechnology*   (2024) 22:498

Page 3 of 12

Fig. 1 Cell-inspired biorthogonal compartmental microparticles (BCMs) encapsulated with biorthogonal reaction agents for tumor therapy. **a** Biomimetic construction of biorthogonal compartmental microparticles (BCM$_{ICG/DOX}$) loaded with TCO-DOX and Tz-ICG via microfluidic electrospray. **b** The therapeutic mechanism of the BCM$_{ICG/DOX}$. (i) After being injected into the tumor site, BCMs exert potent PTT effects upon 808 nm light irradiation based on the intrinsic photothermal performance of Tz-ICG. (ii) Subsequently, TCO-DOX and Tz-ICG are released gradually, initiating a biorthogonal reaction that activates chemotherapy. As a result, the BCM$_{ICG/DOX}$ could efficiently eliminate the cancer cells to prevent the tumor's growth through a combination of PTT and biorthogonal chemotherapy

employed to fabricate various microcarriers with desired features [45–47]. Therefore, inspired by the cell structure and employing the bioorthogonal reaction and microfluidic electrospray technology, it is conceivable that by constructing compartmental microcarriers, different biorthogonal drugs can be loaded separately, and sequential release can be achieved for efficient tumor therapy.

Herein, the biorthogonal compartmental microparticles (BCMs) were fabricated for biorthogonal drug loading, activation, and combination cancer therapy. The core and shell of the microparticles (BCM$_{ICG/DOX}$)

encapsulated a prodrug cyclooctene-modified doxorubicin (TCO-DOX) and an activator tetrazine-modified indocyanine green (Tz-ICG), respectively. Upon application at the tumor site, the BCM$_{ICG/DOX}$ exhibited efficient PTT capability due to the inherent photothermal properties of Tz-ICG. Subsequently, TCO-DOX and Tz-ICG were sequentially released from the core and the shell of the microparticles, triggering a specific inverse electron-demand Diels–Alder (IEDDA) reaction for DOX activation [48, 49]. This activated the efficacy of DOX, enabling effective chemotherapy. Notably, the strategy of prodrug

Zhang *et al. Journal of Nanobiotechnology*   (2024) 22:498

Page 4 of 12

modification could greatly reduce the systemic toxicity of DOX. Given these attributes, the $BCM_{ICG/DOX}$ effectively eradicated tumor cells in vitro and significantly inhibited tumor growth through the synergistic combination of bioorthogonal chemotherapy and PTT, demonstrating favorable safety. These results underscored the potential of BCMs as optimal vehicles for drug delivery, providing a versatile and efficient therapeutic platform for diverse biomedical applications.

Results and discussion

In a typical experiment, BCMs were prepared through a two-step microfluidic electrospray process based on a glass capillary microfluidic device (Fig. 2a, d and Figure S1). Firstly, microparticles (CM_{ICG}) composed of methacrylate gelatin (GelMA) and Tz-ICG were fabricated as the core of BCMs. Briefly, the mixture of GelMA and Tz-ICG was pumped into a capillary microfluidic device to generate droplets, which were collected into liquid nitrogen and then further crosslinked by ultraviolet (UV) light to obtain the CM_{ICG} (Fig. 2a and Figure S1a). Microparticles collected in liquid nitrogen before UV polymerization were free from droplet fusion and cleaning processes, unlike traditional methods, where droplets are collected in an oil phase [50]. Microparticles without drug loading (CM_B) were fabricated as a control. The successful preparation of the microparticles was verified by observing under confocal laser scanning microscopy

(CLSM) and scanning electron microscopy (SEM). As shown in Fig. 2b and Figure S2–S3, both CM_B and CM_{ICG} have regular spherical shapes, with a diameter of 77.6 ± 2.8 μm and 74.9 ± 3.5 μm, respectively. Owing to the loading of Tz-ICG, the CM_{ICG} displayed strong red fluorescence under the excitation light through CLSM, while it could not be observed in CM_B (Fig. 2b). The spherical morphology of the microparticles was observed using SEM, with a notable decrease in average diameter observed following dehydration (Fig. 2c). Subsequently, the above core microparticles were mixed with sodium alginate (Alg) solution and pumped into another capillary microfluidic device to fabricate the BCMs after electrospray and crosslinking with $CaCl_2$ (Fig. 2d and Figure S1b). The compartmental structure of the BCMs with TCO-DOX in the outer core and Tz-ICG in the inner layer was prepared and denoted as $BCM_{ICG/DOX}$. Of note, TCO-DOX was synthesized according to the previous reports. The ^1H NMR spectra of DOX, (2E)-TCO-PNB, and TCO-DOX and the mass spectrum of TCO-DOX are shown in Figure S4–S8, indicating the successful synthesis of TCO-DOX. By careful design according to previous work [51], BCMs containing a single core were fabricated. It could be seen that the inner core and the outer layer of $BCM_{ICG/DOX}$ displayed a red and green color, respectively, due to the fluorescence of Tz-ICG and TCO-DOX under CLSM (Fig. 2e). As shown in Fig. 2f, g and Figure S9, the BCMs had regular spherical shapes
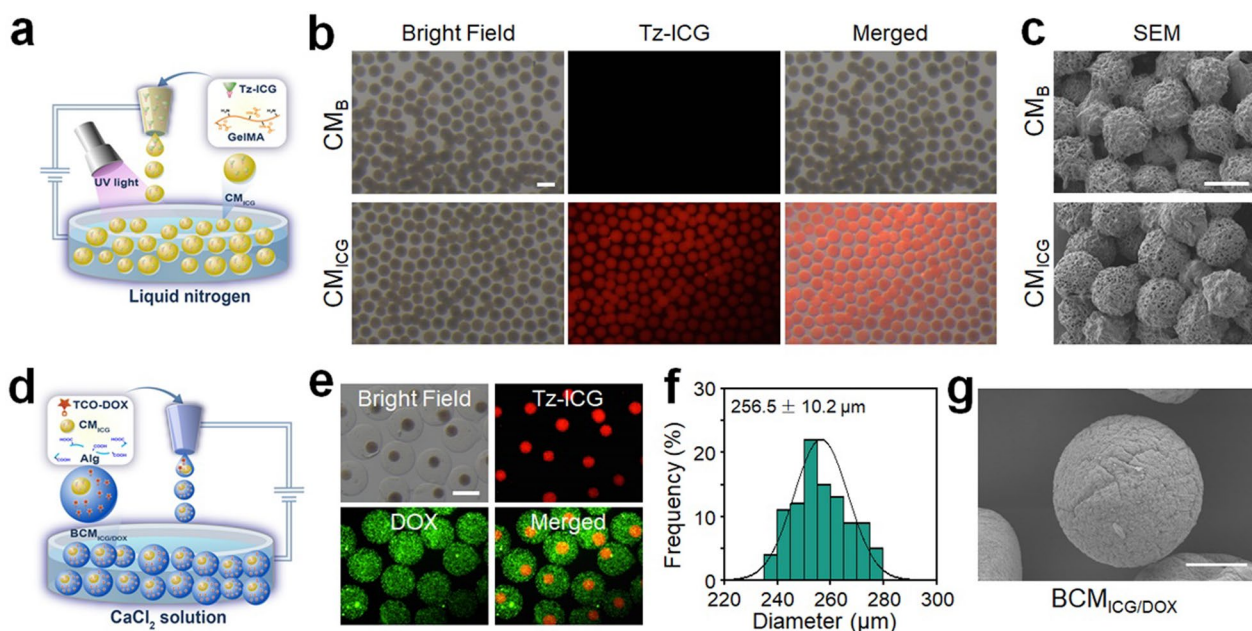

Fig. 2 Characterization of BCMs. **a** Schematic diagram of the preparation process of CMs. **b** Optical and fluorescent images of CM_B and CM_{ICG}. Scale bar: 100 μm. **c** SEM images of CM_B and CM_{ICG}. Scale bar: 25 μm. **d** Schematic diagram of the preparation process of BCMs. **e** Optical and fluorescent images of $BCM_{ICG/DOX}$. Scale bar: 250 μm. **f** Size distribution of $BCM_{ICG/DOX}$. **g** SEM image of $BCM_{ICG/DOX}$. Scale bar: 50 μm

with a diameter of around 260 µm. These results verified the successful fabrication of biorthogonal BCMs.

Indocyanine green (ICG) is a kind of photothermal reagent that is widely used in PTT [52, 53]. As a variant of ICG, it was hypothesized that Tz-ICG might also exhibit photothermal properties. Therefore, a thorough examination of the photothermal effects of Tz-ICG-loaded BCMs was conducted. Figure 3a illustrates the substantial temperature increase of both BCM_{ICG} and $BCM_{ICG/DOX}$ under 808 nm laser irradiation, with a notable rise observed after 3 min (Δ42.2 °C for BCM_{ICG} and Δ41.1 °C for $BCM_{ICG/DOX}$). Conversely, BCM_B and BCM_{DOX} (without Tz-ICG) showed minimal temperature variations under the same conditions. Additionally, increasing the light power intensity notably enhanced the photothermal effect of $BCM_{ICG/DOX}$, as depicted in Fig. 3b. Furthermore, $BCM_{ICG/DOX}$ exhibited consistent thermal stability after five near-infrared (NIR)-On/Off cycles, as shown in Fig. 3c, indicating the sustained photothermal effect of these microparticles. Thermal images visually depict the

photothermal heating process induced by NIR in both BCM_{ICG} and $BCM_{ICG/DOX}$ (Fig. 3d–f and Figure S10). These findings collectively underscore the robustness of the photothermal performance of Tz-ICG-loaded microparticles, laying the foundation for subsequent PTT investigations.

As shown in Figure S11 and Figure S12, Tz-ICG and TCO-DOX have similar absorption and fluorescence spectra with ICG and DOX, respectively. Thus, ICG and DOX was used to load into the BCMs to monitor the drug loading and release processes. Through UV–vis–NIR spectrometer detection and calculating by the standard curves of ICG and DOX (Figure S11), the loading contents of BCMs were 0.15 µg/mg for DOX and 0.20 µg/mg for ICG. Then, the drug-release behaviors of BCMs were investigated. As shown in Fig. 3g, DOX loaded at the outer layer quickly released from BCMs with an 80.9% cumulative release content within 12 h. However, the ICG loaded in the core displayed much slower release behaviors, which could be directly seen from the images
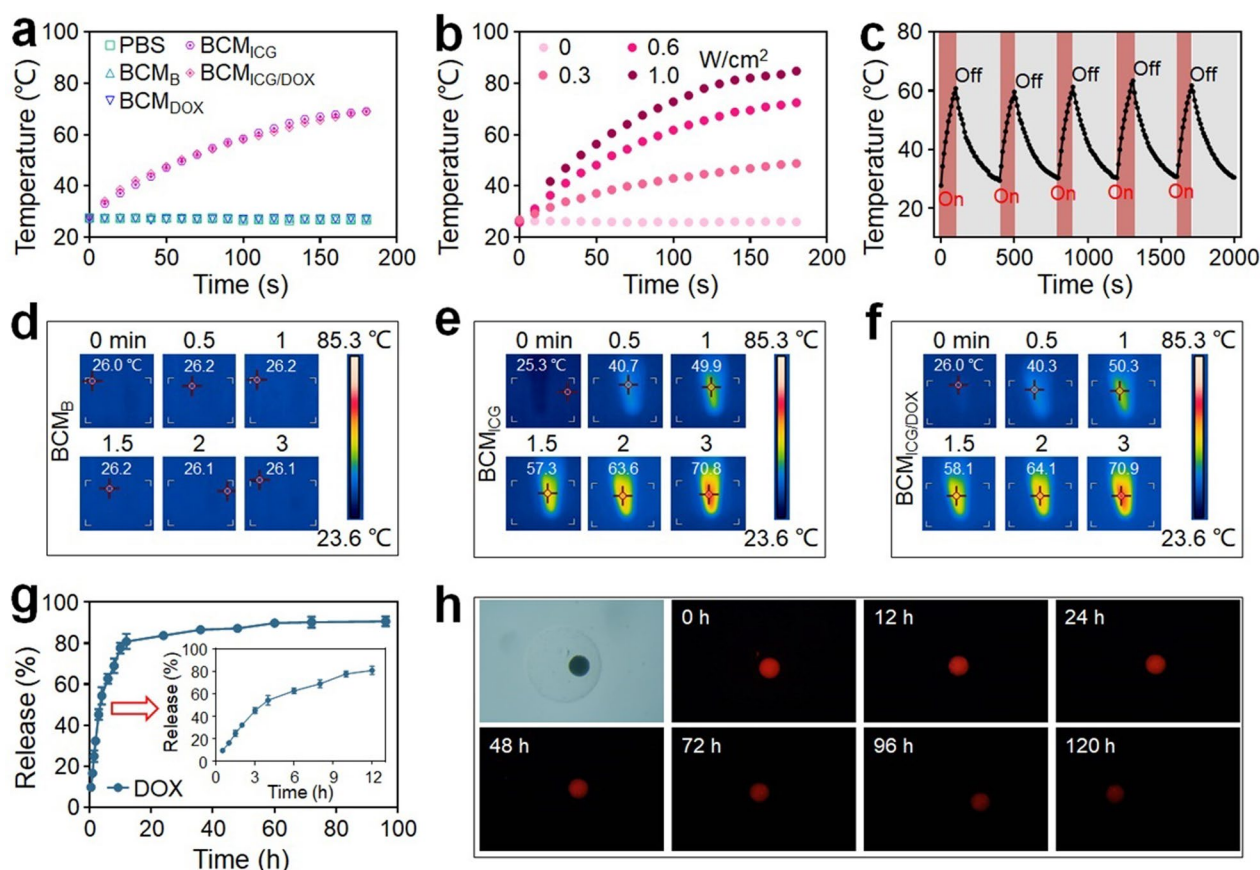

Fig. 3 Photothermal effects and in vitro drug release of BCMs. **a** Photothermal heating curves of different BCMs under 808 nm laser irradiation (0.6 W cm^{-2}). **b** Photothermal heating curves of $BCM_{ICG/DOX}$ with different laser power densities. **c** Temperature variation of $BCM_{ICG/DOX}$ with five 808 nm laser On/Off cycles (0.6 W cm^{-2}, On for 100 s and Off for 300 s). **d–f** Infrared thermal images of BCM_B, BCM_{ICG}, and $BCM_{ICG/DOX}$ under irradiation (0.6 W cm^{-2}). **g** DOX release profile. **h** Images showing ICG release

Zhang *et al. Journal of Nanobiotechnology*   (2024) 22:498

Page 6 of 12

(Fig. 3h). Within 48 h, the ICG-loaded microparticle still had strong fluorescence intensity and lasted until 120 h. Such results demonstrated that the BCMs possess the ability to progressively release drugs, which could be beneficial to the gradual activation of drugs and longstanding therapy against cancer cells.

Following this, the in vitro anti-cancer efficacy of $BCM_{ICG/DOX}$ was assessed using cell counting kit-8 (CCK8) assay and live/dead staining analysis. Initially, the cytotoxicity of TCO-DOX was evaluated both before and after activation by Tz-ICG. In Fig. 4a, free DOX demonstrated potent cytotoxicity with an IC_{50} of 0.339 µM, whereas TCO-DOX exhibited reduced cytotoxicity, with an IC_{50} of 8.146 µM. Upon bioorthogonal activation via IEDDA between TCO-DOX and Tz-ICG (Figure S13), the therapeutic efficacy of TCO-DOX improved, leading to a significant decrease in IC_{50} to 0.423 µM. Importantly, Tz-ICG showed minimal cytotoxicity (Figure S14), affirming the feasibility and effectiveness of the biorthogonal activation reaction. Next, $BCM_{ICG/DOX}$ was added to the upper chamber of a 24-well transwell plate, where

melanoma B16F10 cells were cultured in the lower chamber (Fig. 4b). Following a 5-min irradiation period, the $BCM_{ICG/DOX}$ was then incubated with the B16F10 cells for 24 h before assessing cell viability using the CCK8 assay. As depicted in Fig. 4c, BCM_B and BCM_{ICG} had negligible impact on cell proliferation, while BCM_{DOX} exhibited slight inhibition of cancer cells. In contrast, treatment with $BCM_{ICG/DOX}$ without irradiation demonstrated significantly stronger cytotoxicity against cancer cells compared to BCM_{DOX} alone. Additionally, BCM_{ICG} with photothermal effects (BCM_{ICG} (+)) displayed enhanced cell-killing performance compared to BCM_{ICG} without NIR irradiation. Importantly, the $BCM_{ICG/DOX}$ (+) treatment group exhibited the most effective inhibition of B16F10 cells, attributed to the combined effects of biorthogonal drug activation and photothermal therapy. Live/dead staining consistently supported these findings (Fig. 4d), confirming the outstanding in vitro anticancer effectiveness of $BCM_{ICG/DOX}$, achieved through the combination of PTT and biorthogonal-activated chemotherapy.
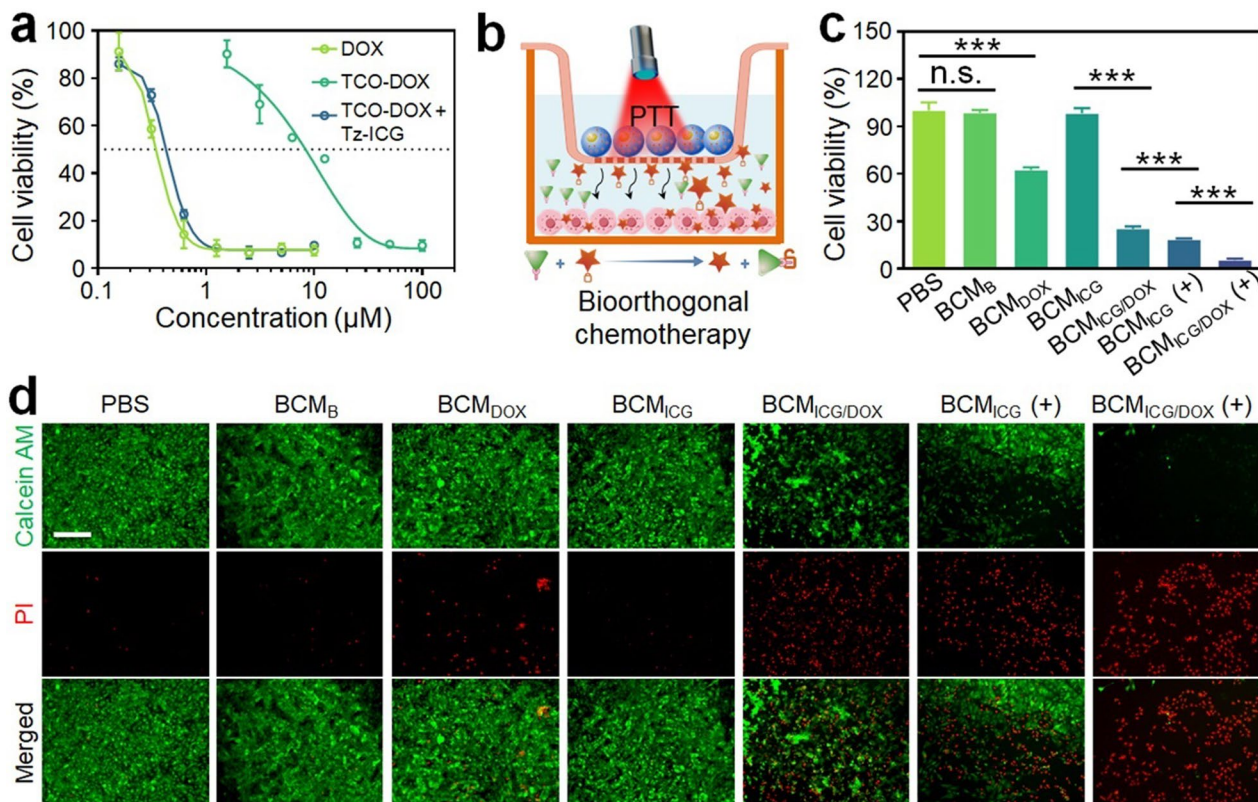

Fig. 4 In vitro antitumor efficacy of BCMs. **a** CCK8 assay of B16F10 cells after incubation with different agents for 24 h. **b** Diagram of the treatment of BCMs against B16F10 cells. **c** CCK8 assay of B16F10 cells after incubation with different BCMs with or without irradiation for 24 h. **d** Live/dead staining of B16F10 cells after incubation with different BCMs with or without irradiation for 24 h (Scale bar: 100 µm). (+) indicated with irradiation (808 nm, 0.6 W cm^{-2}, 5 min). All the cell experiments had three independent replicates (n = 3). Data are presented as the mean ± SD. n. s.: no significance, *p < 0.05, **p < 0.01, ***p < 0.001

The in vivo antitumor effect of $BCM_{ICG/DOX}$ was further evaluated against a subcutaneous melanoma mouse model. The treatment schedule was schematized in Fig. 5a. Then, the in vivo photothermal ability of the microparticles was investigated and the results were displayed in Fig. 5b and Figure S15. The irradiation tumor sites of the BCM_{ICG} and $BCM_{ICG/DOX}$ treatment groups showed significant temperature increases in 5 min, which contributed to the PTT. By contrast, in the PBS and BCM_{DOX} treatment groups, the temperature increases at the tumor sites were within the safe range after irradiation. After that, the tumor volume of each group

was recorded and the results indicated that the PBS and BCM_{ICG} treatment without irradiation cannot suppress the tumor growth due to the unlimited proliferation of melanoma B16F10 cells (Fig. 5c). Compared with the slight inhibition of tumors by the free DOX and BCM_{DOX} treatments, the $BCM_{ICG/DOX}$ group displayed much better anti-tumor efficacy because of the gradually released Tz-ICG and TCO-DOX and biorthogonal reaction between them, thereby activating chemotherapy. Besides, the PTT of BCM_{ICG} could also evidently influence tumor growth. Of note, the $BCM_{ICG/DOX}$ with NIR light irradiation led to the most tumor inhibition effects (Fig. 5d,
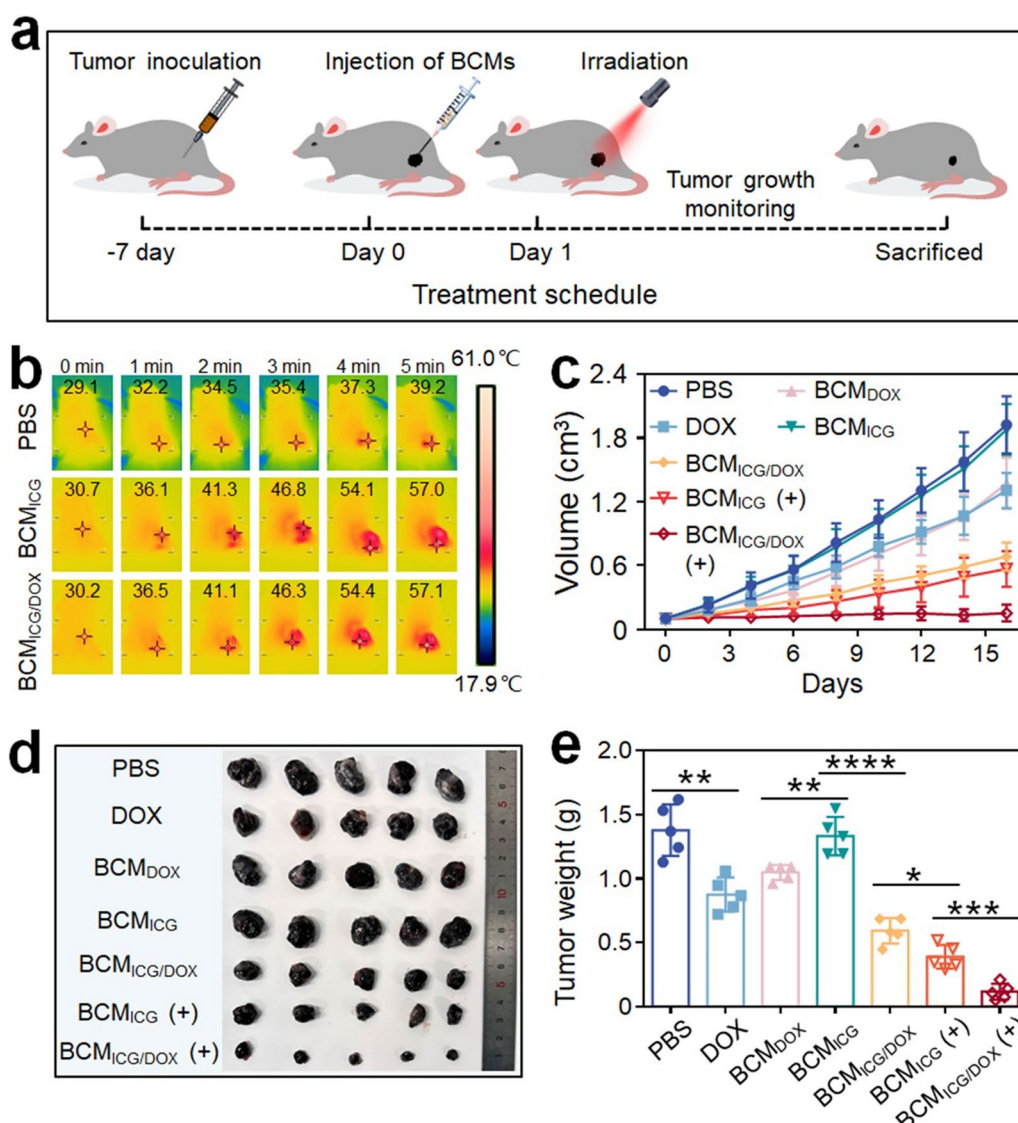

Fig. 5 In vivo anti-tumor performance of BCMs. **a** Schematic illustration of the treatment processes. **b** Infrared thermal images of mice with different treatments and under irradiation for 5 min (0.6 W cm^{-2}). **c** Tumor growth curves of mice after different treatments. **d**, **e** Photograph and tumor weights of B16F10 tumors after different treatments on day 16. Each experiment group has 5 mice (n = 5). Data are presented as the mean ± SD. *p < 0.05, **p < 0.01, ***p < 0.001

Zhang *et al. Journal of Nanobiotechnology*   (2024) 22:498

Page 8 of 12

e). These results demonstrated that the biorthogonal chemotherapy and PTT could achieve potent anti-tumor effects for tumor therapy.

In addition, hematoxylin and eosin (H&E) and terminal-deoxynucleotidyl transferase-mediated nick end labeling (TUNEL) staining analyses on tumor slices were examined to reveal the anti-tumor mechanisms. As anticipated, the H&E staining results indicated that the control and BCM_{ICG} groups without irradiation didn't influence the proliferation of the tumor cells, which were densely populated without apparent cellular nuclear crumbles or disappears (Fig. 6a). In contrast, the $BCM_{ICG/DOX}$ (+) treatment resulted in significant damage to tumor cells in comparison with other groups. Besides, the TUNEL staining results also verified that the $BCM_{ICG/DOX}$ (+) treatment induced the highest apoptosis in tumor tissues (Fig. 6b), indicating the effectiveness of the combination of PTT and biorthogonal chemotherapy. Moreover, the mice were all alive and their body weight increased

during the experiments (Figure S16), except that obvious body weight loss could be seen in the DOX treatment group due to its systemic toxicity after intravenous injections. In addition, no significant histological variations were found in the tissue sections of the major organs in different treatments (Fig. 6c). These results confirmed the good biocompatibility of the BCMs.

Conclusion

In summary, we have fabricated bio-inspired biorthogonal compartmental microparticles ($BCM_{ICG/DOX}$) from microfluidics for step-wise loading and releasing of biorthogonal reaction agents for synergistic tumor therapy. TCO-DOX and Tz-ICG were encapsulated in the outer layer and core of the $BCM_{ICG/DOX}$, respectively. Thus, the drugs could be released from $BCM_{ICG/DOX}$ in a step-wise mode. When applied at the tumor site, the quickly released TCO-DOX from the out layer of the microparticles could be gradually activated by
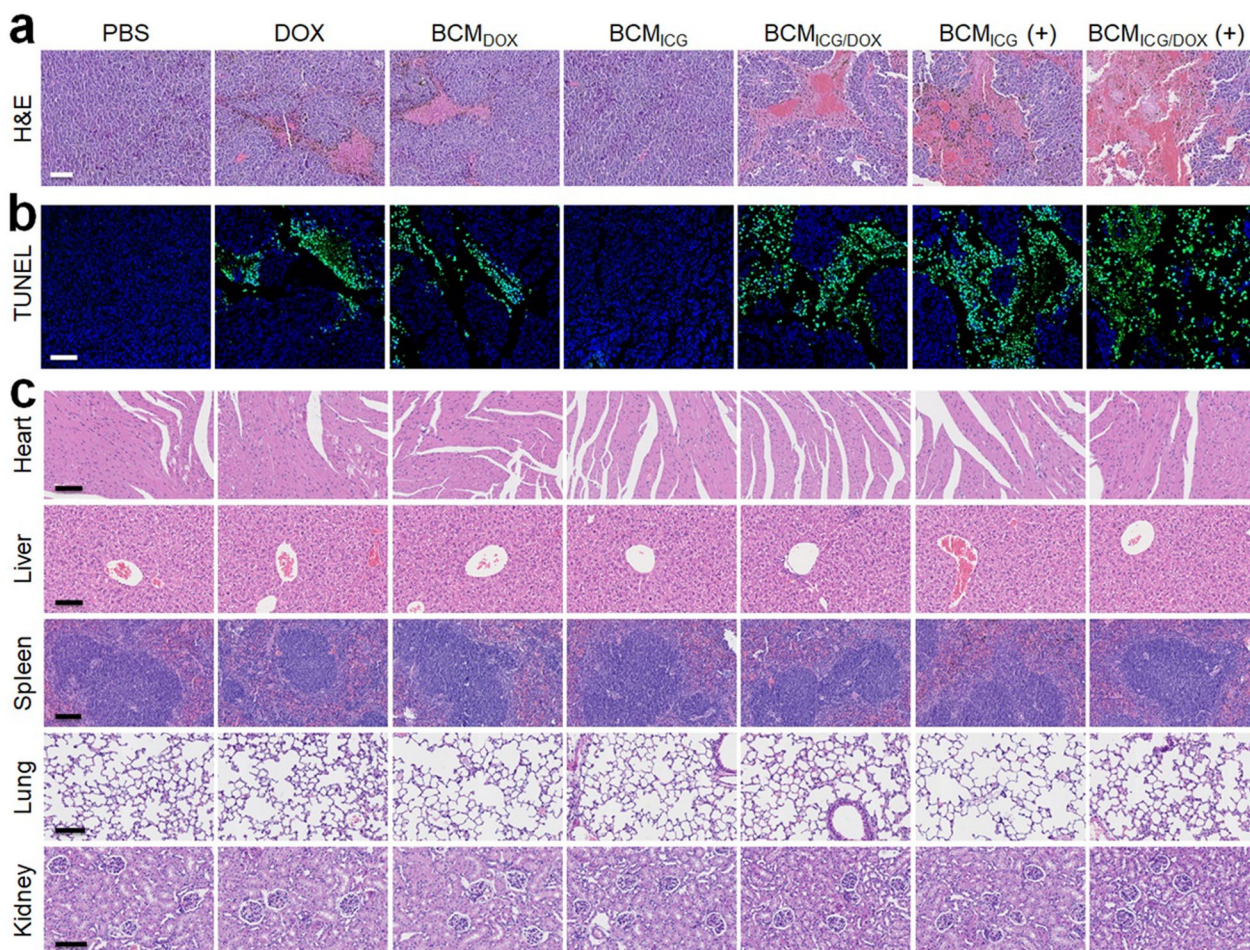

Fig. 6 H&E and TUNEL analyses. **a**, **b** H&E and TUNEL staining analyses of tumors after different treatments. **c** H&E staining analyses of major organs after different treatments. Scale bars: 50 µm

the Tz-ICG released from the core through an IEDDA bioorthogonal reaction, thereby restoring DOX's cytotoxicity and enabling potent chemotherapy. Additionally, the Tz-ICG encapsulated in the microcarriers exhibited efficient PTT ability under NIR light irradiation. Consequently, the resulting $BCM_{ICG/DOX}$ showcased a substantial cytotoxic effect on tumor cells and effectively suppressed tumor growth through a synergistic combination of PTT and chemotherapy, with minimal systemic toxicity observed. Thus, the developed BCMs offer an effective and versatile delivery system for bioorthogonal drug activation and delivery, holding significant potential for tumor therapy. The limitations associated with the developed system involve the fabrication processes and the further assessment of the therapeutic efficacy. The two-step microfluidic electrospray process may be improved with the adoption of a one-step process for more effective mass production of the microparticles. Besides, additional testing, including large animal experiments, is necessary prior to the clinical application of this system.

Materials and methods

Materials

Calcium chloride ($CaCl_2$), diisopropylethylamine (DIPEA), doxorubicin hydrochloride (DOX·HCl), and sodium alginate (Alg) were purchased from Macklin, while gelatin was obtained from Sigma-Aldrich. Me-tetrazine-ICG (Tz-ICG) and (E)-Cyclooct-2-en-1-yl (4-nitrophenyl) carbonate ((2E)-TCO-PNB) were acquired from Confluore Biotechnology Co. Ltd. The calcein-AM/propidium iodide (PI) staining assay kit was obtained from Meilunbio, Co., Ltd., and the CCK8 assay kit was procured from Beyotime Biotechnology Co. Ltd.

Synthesis of TCO-DOX

The compound (2E)-TCO-PNB (15 mg, 0.05 mmol) was initially dissolved in 2 mL of dimethylformamide. Following this, DIPEA (64.5 mg, 0.50 mmol) and DOX·HCl (35 mg, 0.06 mmol) were added to the solution. The mixture was stirred in darkness at 30 °C for 3 days. Subsequently, 10 mL of water was added, and the resulting mixture was extracted with EtOAc (4×50 mL). The combined organic phase was then washed sequentially with saturated $NaHCO_3$ (3×50 mL), distilled water (3×50 mL), and saturated NaCl solution (3×50 mL). It was subsequently dried using anhydrous Na_2SO_4 for 2 h. Finally, the solvent was removed under reduced pressure, leaving behind a residue that underwent purification via column chromatography (CH_2Cl_2: MeOH = 98: 2) to yield the TCO-DOX (22 mg, 63.5%). ^1H NMR ($CDCl_3$, 400 MHz), δ (ppm): 14.03 (s, 1H), 13.30 (s, 1H), 8.10–8.06 (d, 1H), 7.83 (t, 1H), 7.46–7.40 (d, 1H), 5.90–5.00 (m, 6H), 4.80 (d, 2H), 4.57 (s, 1H), 4.20 (m, 1H), 4.13 (s, 4H), 3.92 (s, 1H), 3.77–3.64 (m, 2H), 3.37–3.28 (d, 1H), 3.15–3.00 (m, 2H), 2.48 (s, 1H), 2.41–2.31 (d, 1H), 2.28–2.16 (m, 1H), 2.11–1.77 (m, 10H).

Preparation of BCMs

The preparation of BCMs was a two-step process by using microfluidic electrospray technology. Firstly, the microparticles in the core were prepared. The pregel solution containing methacrylate gelatin (GelMA, 10 wt%) and Tz-ICG (10 mg mL^{-1}) was pumped into a capillary microfluidic device. The orifice of the cylindrical glass capillary tube was 60 μm. Set the injection pump flow rate to 0.5 mL h^{-1} and the high voltage supply voltage to 6 kV. Then, the droplets generated under the high-voltage electric field were collected into liquid nitrogen and further crosslinked by UV light to obtain the microparticles. After that, the above microparticles were added to the Alg solution (2 wt%) containing TCO-DOX (0.5 mg mL^{-1}). After the solution was homogenous, it was pumped into a capillary microfluidic device with an orifice of 150 μm. The flow rate and voltage were set as 0.5 mL h^{-1} and 4 kV. Subsequently, the BCMs were collected and solidified in a $CaCl_2$ solution (2 wt%) through microfluidic electrospray. By changing the drugs loaded in the core or the outer layer, various types of BCMs could be fabricated.

Characterizations

A stereomicroscope (Olympus BX51, Tokyo, Japan) was utilized for optical imaging of the microparticles, and a field emission SEM (SU8010, Hitachi, Japan) was employed to examine the surface morphology and structure of the microparticles. Before imaging with an SEM, the microparticles underwent a sequential dehydration process using ethanol solutions with concentrations of 70%, 80%, 90%, and 100%, followed by supercritical drying.

The photothermal effect of BCMs

The photothermal properties of BCMs were assessed using 808 nm laser irradiation. Various BCMs underwent laser irradiation, and the resulting temperature rise was monitored over time using a thermal imager (FLIR E5-XT). Additionally, the photothermal behavior of BCMs was evaluated by adjusting the laser power intensity (0, 0.3, 0.6, and 1.0 W cm^{-2}). Furthermore, the photothermal stability of BCMs was investigated through five "On–Off" cycles, during which the BCMs were subjected to 100 s of laser irradiation (laser On, 0.6 W cm^{-2}) followed by natural cooling without irradiation for 300 s (laser Off).

Zhang *et al. Journal of Nanobiotechnology*   (2024) 22:498

Page 10 of 12

Drug release study

Firstly, the absorption and fluorescence spectra of DOX, TCO-DOX, ICG, and Tz-ICG were investigated. The absorption spectra of DOX and TCO-DOX from 300 to 600 nm were measured by a UV–Vis-NIR spectrophotometer. The absorption spectra of ICG and Tz-ICG from 300 to 900 nm were also measured. The fluorescence spectra of DOX and TCO-DOX, ranging from 500 to 700 nm, were obtained using a Cary Eclipse fluorescence spectrophotometer with excitation at a wavelength of 480 nm. The fluorescence spectra of ICG and Tz-ICG from 790 to 860 nm were measured with 780 nm excitation. Then, to facilitate testing and operation, the release profiles of ICG and DOX were examined from BCM_{ICG} and BCM_{DOX}, respectively. BCM_{DOX} was placed into a 50 mL tube containing 20 mL of PBS for DOX release assessment. Subsequently, the tube underwent oscillation in a chamber with a velocity of 100 rpm at 37 ℃. At predefined intervals, 1 mL of the release medium was withdrawn, and an equal volume of PBS was replenished. The released DOX in the collected solution was quantified using a UV–Vis-NIR spectrophotometer. Similarly, BCM_{ICG} was submerged in PBS and subjected to oscillation. At specified time points, BCM_{ICG} was observed under a CLSM to directly monitor the release of ICG.

In vitro antitumor study

In each well of the lower compartment of a 24-well transwell plate, 5×10^4 B16F10 cells were seeded and allowed to attach for 12 h. Following the attachment, various BCMs were introduced into the upper compartment of the transwell plate. The BCM_{ICG} or $BCM_{ICG/DOX}$ treatment groups underwent partial exposure to NIR laser irradiation for 5 min, followed by a 24 h incubation period, while the remaining groups were kept in the dark for the entire 24 h. Subsequently, to assess the in vitro anti-tumor effects of BCMs on cancer cells, live/dead staining and a CCK8 assay were performed. For live/dead staining, the treated cells were incubated with the Calcein-AM/PI agent, and their viability was observed under a fluorescence microscope. Simultaneously, the CCK8 reagent was added to the cells for 2 h, and the absorbance at 450 nm was measured using a microplate reader.

Tumor inhibition in vivo

After inoculating the mouse's right flank with 1×10^6 B16F10 cells via subcutaneous injection, tumor growth was permitted until the tumor volume approached 100 mm³. Subsequently, to assess the in vivo photothermal efficacy of the microparticles, PBS, BCM_{DOX}, BCM_{ICG}, and $BCM_{ICG/DOX}$ were intratumorally injected at the tumor sites. Following injection, the tumors were exposed to the laser for 5 min, and the resulting temperature elevations were monitored using an infrared thermal imager. The mice were then randomly divided into 7 groups (n=5): control, free DOX, BCM_{DOX} (no irradiation), BCM_{ICG} (no irradiation), $BCM_{ICG/DOX}$ (no irradiation), BCM_{ICG} (with irradiation), and $BCM_{ICG/DOX}$ (with irradiation). Record the body weight and tumor volume every 2 days. Finally, euthanasia was performed after 16 days, and primary organs and tumors were taken, fixed with 4% (v/v) paraformaldehyde, and cut into 5 μm-thick slices for H&E and TUNEL staining. The power intensity of the 808 nm laser was set at 0.6 W cm^{-2} for 5 min. The animal studies were permitted by the Ethical Committee of Wenzhou Institute, University of Chinese Academy of Sciences (approval WIUCAS23062105) and strictly according to the Laboratory Animal Care and Use Guidelines.

Statistical analysis

All statistical data are expressed as the mean ± standard deviations. Statistical evaluation was analyzed using unpaired Student's t-test or one-way ANOVA, and a p-value < 0.05 was considered statistically significant. n. s.: no significance, *p < 0.05, **p < 0.01, ***p < 0.001, ****p < 0.0001.

Supplementary Information

The online version contains supplementary material available at https://doi.org/10.1186/s12951-024-02778-w.

Supplementary material 1.

Availability of data and materials
No datasets were generated or analysed during the current study.

Declarations

Ethics approval and consent to participate
The animal studies were permitted by the Ethical Committee of Wenzhou Institute, University of Chinese Academy of Sciences (approval

Author details
[1]Department of Gastrointestinal Surgery, The First Affiliated Hospital, Wenzhou Medical University, Wenzhou 325035, China. [2]Oujiang Laboratory (Zhejiang Lab for Regenerative Medicine, Vision and Brain Health), Wenzhou Institute, University of Chinese Academy of Sciences, Wenzhou 325001, China. [3]Department of Rheumatology and Immunology, Nanjing Drum Tower Hospital, School of Biological Science and Medical Engineering, Southeast University, Nanjing 210096, China. [4]Shanghai Xuhui Central Hospital, Zhongshan-Xuhui Hospital, and the Shanghai Key Laboratory of Medical Epigenetics, International Co-Laboratory of Medical Epigenetics and Metabolism (Ministry of Science and Technology), Institutes of Biomedical Sciences, Fudan University, Shanghai 200032, China.

References
1. Jaffray DA, Knaul F, Baumann M, et al. Harnessing progress in radiotherapy for global cancer control. Nature Cancer. 2023;4(9):1228–38.
2. Huang C, Wang X, Wang Y, et al. Sirpα on tumor-associated myeloid cells restrains antitumor immunity in colorectal cancer independent of its interaction with CD47. Nature Cancer. 2024;5:500–16.
3. Zhang Q, Kuang G, Wang L, et al. Tailoring drug delivery systems by microfluidics for tumor therapy. Mater Today. 2024;73:151–78.
4. Li J, Chen Z, Bai Y, et al. First-line sugemalimab with chemotherapy for advanced esophageal squamous cell carcinoma: a randomized phase 3 study. Nat Med. 2024;30:740–8.
5. Kuboki Y, Fakih M, Strickler J, et al. Sotorasib with panitumumab in chemotherapy-refractory KRASG12C-mutated colorectal cancer: a phase 1b trial. Nat Med. 2024;30(1):265–70.
6. Pomeroy AE, Schmidt EV, Sorger PK, et al. Drug independence and the curability of cancer by combination chemotherapy. Trends in cancer. 2022;8(11):915–29.
7. Chabner BA, Roberts TG Jr. Chemotherapy and the war on cancer. Nat Rev Cancer. 2005;5(1):65–72.
8. Baryakova TH, Pogostin BH, Langer R, et al. Overcoming barriers to patient adherence: the case for developing innovative drug delivery systems. Nat Rev Drug Disc. 2023;22(5):387–409.
9. Mitchell MJ, Billingsley MM, Haley RM, et al. Engineering precision nanoparticles for drug delivery. Nat Rev Drug Disc. 2021;20(2):101–24.
10. Gao D, Chen T, Chen S, et al. Targeting hypoxic tumors with hybrid nanobullets for oxygen-independent synergistic photothermal and thermodynamic therapy. Nano-Micro Lett. 2021;13(1):1–21.
11. Lan Z, Liu W-J, Yin W-W, et al. Biomimetic MDSCs membrane coated black phosphorus nanosheets system for photothermal therapy/photodynamic therapy synergized chemotherapy of cancer. J Nanobiotechnol. 2024;22(1):174.
12. Guo S, Gu D, Yang Y, et al. Near-infrared photodynamic and photothermal co-therapy based on organic small molecular dyes. J Nanobiotechnol. 2023;21(1):348.
13. Ouyang J, Zhang Z, Deng B, et al. Oral drug delivery platforms for biomedical applications. Mater Today. 2023;62:296–326.
14. Sun L, Liu H, Ye Y, et al. Smart nanoparticles for cancer therapy. Signal Transduct Target Ther. 2023;8(1):418.
15. Feng C, Ouyang J, Tang Z, et al. Germanene-based theranostic materials for surgical adjuvant treatment: inhibiting tumor recurrence and wound infection. Matter. 2020;3(1):127–44.
16. Luo M, Dorothy Winston D, Niu W, et al. Bioactive therapeutics-repair-enabled citrate-iron hydrogel scaffolds for efficient post-surgical skin cancer treatment. Chem Eng J. 2022;431: 133596.
17. Zhang H, Liu Y, Chen C, et al. Responsive drug-delivery microcarriers based on the silk fibroin inverse opal scaffolds for controllable drug release. Appl Mater Today. 2020;19: 100540.
18. Shou X, Liu Y, Wu D, et al. Black phosphorus quantum dots doped multifunctional hydrogel particles for cancer immunotherapy. Chem Eng J. 2021;408: 127349.
19. Zhu T, Liang D, Zhang Q, et al. Curcumin-encapsulated fish gelatin-based microparticles from microfluidic electrospray for postoperative gastric cancer treatment. Int J Biol Macromol. 2023;254(Pt 1): 127763.
20. Zhang Q, Kuang G, Li W, et al. Stimuli-responsive gene delivery nanocarriers for cancer therapy. Nano-Micro Lett. 2023;15(1):44.
21. Li J, Zhu T, Jiang Y, et al. Microfluidic printed 3D bioactive scaffolds for postoperative treatment of gastric cancer. Mater Today Bio. 2024;24: 100911.
22. Ji W, Zhang Y, Deng Y, et al. Nature-inspired nanocarriers for improving drug therapy of atherosclerosis. Regenerat Biomater. 2023;10:rbad069.
23. Gan J, Huang D, Che J, et al. Biomimetic nanoparticles with cell-membrane camouflage for rheumatoid arthritis. Matter. 2024;7(3):794–825.
24. Zhu H, Kong B, Che J, et al. Bioinspired nanogels as cell-free DNA trapping and scavenging organelles for rheumatoid arthritis treatment. Proc Natl Acad Sci. 2023;120(33): e2303385120.
25. Scinto SL, Bilodeau DA, Hincapie R, et al. Bioorthogonal chemistry. Nature Rev Methods Primers. 2021;1(1):30.
26. Richter D, Lakis E, Piel J. Site-specific bioorthogonal protein labelling by tetrazine ligation using endogenous β-amino acid dienophiles. Nat Chem. 2023;15(10):1422–30.
27. Zhang Q, Kuang G, Wang L, et al. Designing bioorthogonal reactions for biomedical applications. Research. 2023;6:0251.
28. Huang C, Zhao C, Deng Q, et al. Hydrogen-bonded organic framework-based bioorthogonal catalysis prevents drug metabolic inactivation. Nat Catal. 2023;6(8):729–39.
29. Chen Z, Li H, Bian Y, et al. Bioorthogonal catalytic patch. Nat Nanotechnol. 2021;16(8):933–41.
30. Oliveira B, Guo Z, Bernardes G. Inverse electron demand diels-alder reactions in chemical biology. Chem Soc Rev. 2017;46(16):4895–950.
31. Srinivasan S, Yee NA, Wu K, et al. SQ3370 activates cytotoxic drug via click chemistry at tumor and elicits sustained responses in injected & non-injected lesions. Adv Ther. 2021;4(3):2000243.
32. Werther P, Yserentant K, Braun F, et al. Bio-orthogonal red and far-red fluorogenic probes for wash-free live-cell and super-resolution microscopy. ACS Cent Sci. 2021;7(9):1561–71.
33. Rossin R, Versteegen RM, Wu J, et al. Chemically triggered drug release from an antibody-drug conjugate leads to potent antitumour activity in mice. Nat Commun. 2018;9(1):1484.
34. Liu Y, Huang Q, Wang J, et al. Microfluidic generation of egg-derived protein microcarriers for 3D cell culture and drug delivery. Sci Bull. 2017;62(18):1283–90.
35. Zhang Q, Wang X, Kuang G, et al. Pt(IV) prodrug initiated microparticles from microfluidics for tumor chemo-, photothermal and photodynamic combination therapy. Bioactive Mater. 2023;24:185–96.
36. Wang H, Zhao Z, Liu Y, et al. Biomimetic enzyme cascade reaction system in microfluidic electrospray microcapsules. Sci Adv. 2018;4(6):eaat2816.
37. Zhang Q, Kuang G, Wang H, et al. Multi-bioinspired MOF delivery systems from microfluidics for tumor multimodal therapy. Adv Sci. 2023;10(33):2303818.
38. Aleman J, Kilic T, Mille LS, et al. Microfluidic integration of regeneratable electrochemical affinity-based biosensors for continual monitoring of organ-on-a-chip devices. Nat Protoc. 2021;16(5):2564–93.
39. Barry R, Ivanov D. Microfluidics in biotechnology. J Nanobiotechnol. 2004;2(1):2.
40. Yang C, Yu Y, Shang L, et al. Flexible hemline-shaped microfibers for liquid transport. Nature Chem Eng. 2024;1(1):87–96.
41. Huang D, Wang J, Nie M, et al. Pollen-inspired adhesive multilobe microparticles from microfluidics for intestinal drug delivery. Adv Mater. 2023;35(28):2301192.
42. Zhi Y, Che J, Zhu H, et al. Glycyrrhetinic acid liposomes encapsulated microcapsules from microfluidic electrospray for inflammatory wound healing. Adv Func Mater. 2023;33(43):2304353.

Zhang *et al. Journal of Nanobiotechnology*   (2024) 22:498

Page 12 of 12

43. Li W, Zhang L, Ge X, et al. Microfluidic fabrication of microparticles for biomedical applications. Chem Soc Rev. 2018;47(15):5646–83.
44. Jiang Z, Shi H, Tang X, et al. Recent advances in droplet microfluidics for single-cell analysis. TrAC, Trends Anal Chem. 2023;159: 116932.
45. Kuang G, Zhang Q, Li W, et al. Biomimetic tertiary lymphoid structures with microporous annealed particle scaffolds for cancer postoperative therapy. ACS Nano. 2024;18(12):9176–86.
46. Cai L, Li N, Zhang Y, et al. Microfluidics-derived microcarrier systems for oral delivery. Biomed Technol. 2023;1:30–8.
47. Yang L, Liu Y, Sun L, et al. Biomass microcapsules with stem cell encapsulation for bone repair. Nano-Micro Lett. 2021;14(1):4.
48. Yao Q, Lin F, Fan X, et al. Synergistic enzymatic and bioorthogonal reactions for selective prodrug activation in living systems. Nat Commun. 2018;9(1):5032.
49. Ma Y, Zhou Y, Long J, et al. A high-efficiency bioorthogonal tumor-membrane reactor for in situ selective and sustained prodrug activation. Angew Chem Int Ed. 2024;136(10): e202318372.
50. Yang L, Wang X, Yu Y, et al. Bio-inspired dual-adhesive particles from microfluidic electrospray for bone regeneration. Nano Res. 2023;16(4):5292–9.
51. Zhong J, Zhang Q, Kuang G, et al. Multicomponent microspheres with spatiotemporal drug release for post-surgical liver cancer treatment and liver regeneration. Chem Eng J. 2023;455: 140585.
52. Hou SS, Yang J, Lee JH, et al. Near-infrared fluorescence lifetime imaging of amyloid-β aggregates and tau fibrils through the intact skull of mice. Nature Biomed Eng. 2023;7(3):270–80.
53. Wang L, Chen P, Pan Y, et al. Injectable photocurable janus hydrogel delivering hiPSC cardiomyocyte-derived exosome for post–heart surgery adhesion reduction. Sci Adv. 2023;9(31):eadh1753.

Publisher's Note